

# Analytical Model for the Linear Energy Transfer of Secondary Protons from Elastic Reactions in Proton Beam Therapy

Benjamin White

*Student ID*

University of Manchester

School of Physics and Astronomy

Work performed in collaboration with *Project Partner*

May 2021

## Abstract

A novel three-dimensional model for the spectrum of secondary protons produced in elastic reactions in a homogeneous water phantom is devised, such that the linear energy transfer, a quantity essential to predicting the biological effect of the beam in proton therapy, can be calculated. By considering the angular and energetic distribution of secondary protons produced by a Gaussian beam of primary protons, an expression for the number of protons reaching an arbitrary point with a given energy is obtained.

Monte Carlo simulations are carried out with GEANT4 to measure the cross section for elastic reactions, and the resulting angular distribution. By modelling the reaction as a two-body kinematic problem, a relationship between the energy of the secondary proton and the angle at which it is produced is obtained. The simulation is then used to produce data to compare with the model.

The model underestimates the number of low energy secondary protons produced, and so fails to accurately predict the LET distribution as a function of depth in the water phantom, especially in the plateau region before the Bragg peak, where the model underestimates LET by  $2 \text{ keV } \mu\text{m}^{-1}$ . Potential reasons for the discrepancy are discussed, as well as ways to extend the model to include secondary protons from inelastic collisions.

# 1 Introduction

The wealth of clinical knowledge of the biological effectiveness of radiotherapy treatments comes from patients treated with X-rays. We therefore require a way to compare the efficacy of proton or ion-beams (such as carbon ions) to X-rays. This is done using relative biological effectiveness (RBE). RBE is calculated as ratio of the required absorbed dose of some ionizing radiation to that of photons, in order to reach the same biological endpoint. Currently, for proton beams, RBE is treated as a constant of 1.1 [1]. It is known, however, that RBE varies with many quantities of both the target tissue and the beam, such as the tissue type and oxygenation, as well as the linear energy transfer (LET) of the proton beam [2] [3]. It is therefore important to be able to predict LET distributions in a patient when devising a treatment plan in order to reduce the risk of secondary malignancies.

Since LET is difficult to measure in experiments, Monte Carlo particle transport simulations such as FLUKA and GEANT can be used instead to obtain distributions of absorbed dose and LET in patient geometries. Depending on the desired quality of the simulation, this process may take hours. In order to optimise a treatment plan, many iterations of the simulation with different parameters must be carried out, which may be a prohibitively time-consuming process. It is therefore useful to use analytical models to approximate the result of the simulations. A 1997 model by Bortfeld accurately predicts depth-dose curves in water [4]. This model was extended in 2003 by Wilkens and Oelfke to model the LET distribution from protons [5]. They also demonstrated that the model is effective for modelling the LET for spread-out Bragg peaks, where several beams are superimposed to produce a flat region in the depth-dose profile with width equivalent to that of the target tissue.

The Wilkens model however has two significant disadvantages: it fails to consider the lateral spread of the proton beams, and it does not account for the LET of secondary protons produced in nuclear reactions between the proton beam and the target. As the beam propagates through the medium, it diverges causing a penumbra of increased LET off-axis, whilst the Wilkens model is only applicable to the central beam axis. Moreover, it is known that secondary protons have a significant contribution to LET, particularly away from the beam axis [6]. A 2016 model by Sanchez-Parcerisa et al. adds a polynomial correction to the LET caused by primary protons to account for secondary protons [7]. Other particles such as heavy ions, electrons, neutrons and gammas are also produced, but less frequently than secondary protons. Additionally, neutrons and gammas do not contribute to LET since they are not charged particles. This work therefore focuses on secondary protons, however the general method could also be adapted to include other particles.

The authors' previous work followed a similar method to Wilkens, where the energy spectrum of protons at a point is converted into an LET value [8]. It attempted to improve on it by modelling the secondary proton LET. A piecewise model was fitted to secondary proton energy spectra as a function of depth within the simulation geometry. The resulting LET distributions, when com-

bined with the Wilkens model for primary proton LET, resulted in a noticeable improvement in LET distributions when compared to Monte Carlo data, particularly in the plateau region of the Bragg curve. Whilst for a single beam this region is not clinically relevant due to the small amount of dose deposited there, when combining many beams with different energies to produce a spread-out Bragg peak, any discrepancy in the plateau region is compounded. However, the numerous fitting parameters could only be obtained by performing the Monte Carlo simulation in full.

This work therefore attempts to derive a model for the secondary proton spectrum entirely from analytical considerations, such that it may be used independently of the Monte Carlo simulation. The model should be able to fully describe the three-dimensional LET distribution from secondary protons, such that it may be combined with a model for the primary proton LET to produce a complete LET distribution, which could then be used to optimize a treatment plan by maximizing biological effect at the target tissue, whilst minimizing the damage to the surrounding tissue. Accuracy at the end of the beam's range is important, since LET and therefore biological effect peak at the distal edge of the Bragg curve.

This paper is structured as follows: a brief definition of LET is given before deriving the model. Then a description of the Monte Carlo simulation and LET scoring method is given, followed by a presentation of the results and a discussion.

## 2 Theory

The stopping power of a proton as it travels through some medium is defined as

$$S = \left( \frac{dE}{dx} \right)_{el} + \left( \frac{dE}{dx} \right)_{nuc} + \left( \frac{dE}{dx} \right)_{rad} \quad (1)$$

where  $dE$  is the energy lost travelling a distance  $dx$ . The first term corresponds to the energy lost due to inelastic collisions between the proton and the orbital electrons in the medium, the second due to energy lost due to elastic collisions with atoms in the medium, and the third due to radiative processes that can be neglected at clinical energies [9]. The dominant term in (1) is the first. Thus the LET is defined as

$$L = \left( \frac{dE}{dx} \right)_{el}. \quad (2)$$

The LET at a point,  $L(\vec{x})$ , may be calculated from the energy spectrum of protons using

$$L(\vec{x}) = \frac{\int \phi_\varepsilon(\vec{x}) S^2(\varepsilon) d\varepsilon}{\int \phi_\varepsilon(\vec{x}) S(\varepsilon) d\varepsilon}, \quad (3)$$

where  $\phi_\varepsilon(\vec{x})$  is the energy spectrum of the protons (i.e. the number of protons with energy  $\varepsilon$  passing through the point  $\vec{x}$ ).

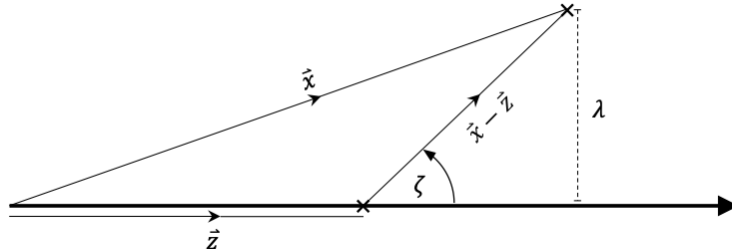


Figure 1: Illustration of the coordinate system used to describe the elastic interactions. The beam axis is depicted with a heavy line.

Secondary protons are produced by two processes during proton beam therapy: *elastic* and *inelastic* reactions, labelled `hadElastic` and `protonInelastic` in GEANT4. Whilst both contribute to the secondary LET, this work focuses on those produced in elastic collisions. The reasoning for this is twofold. First, elastic protons are more prevalent at the end of the beam, where LET is the most significant. This is due to the fact that inelastic reactions require that the primary proton has energy enough to overcome the Coulomb barrier, approximately 8 MeV, whilst at the end of the beam's range, the protons do not have sufficient energy to overcome this, and so elastic reactions dominate. Second, as we demonstrate later, the model becomes greatly simplified when considering only secondary protons produced in elastic reactions, since there exists a unique relationship between the angle at which they are produced and their kinetic energy.

To describe the trajectories of the secondary protons, the coordinate system illustrated in Figure 1 is used.  $\vec{z}$  is the position vector of the elastic interaction site,  $\vec{x}$  is the position vector of the point at which the secondary proton spectrum is calculated,  $\zeta$  is the angle between the beam axis and the trajectory of the secondary proton, and  $\lambda$  is the perpendicular distance between the beam axis and  $\vec{x} - \vec{z}$ . A cylindrical coordinate system is used since the elastic reactions have azimuthal symmetry. Note that we have assumed that all reactions happen along the beam axis. The validity of this assumption is explored in subsection 4.3.

The energy of the secondary protons is more conveniently expressed in terms of the residual range  $r$ . In the continuous slowing down approximation, where the rate of energy loss of the protons with respect to the distance travelled is equal to the stopping power, there exists a unique relationship between the proton kinetic energy  $E$  and the range:

$$r = \alpha E^p, \quad (4)$$

where  $\alpha = 0.022 \text{ mm MeV}^{-p}$  and  $p = 1.77$  are parameters specific to protons in water as determined by Bortfeld [4]. In reality, due to the statistical nature of the process by which protons lose their energy, they will have ranges distributed about  $r$ . This is known as range straggling.

In order to calculate the range spectrum of secondary protons at  $\vec{x}$ ,  $\phi_{\tilde{r}}(\vec{x})$ , we consider the probability of a secondary proton being produced at  $\vec{z}$  at an angle  $\zeta$  such that it has residual range  $\tilde{r}$  when it reaches  $\vec{x}$ . It must therefore be produced with range  $r = |\vec{x} - \vec{z}| + \tilde{r}$ . The spectrum at  $\vec{x}$  is the sum of the contributions from all  $\vec{z}$  between 0 and the maximum range of the beam of primary protons,  $R_0$ , which can be determined from (4).

The probability of producing a secondary proton at some depth is proportional to  $\sigma \times \phi_p$ , where  $\sigma$  is the cross section for the elastic reaction, and  $\phi_p$  is the primary proton spectrum, which is given by Bortfeld as

$$\phi_p(\rho, z) = \frac{1 + \beta(R_0 - z)}{1 + \beta R_0} \exp\left(-\frac{(\rho - (R_0 - z))^2}{2\sigma_{width}^2}\right), \quad (5)$$

where  $\rho$  is used to denote the primary residual range, rather than  $r$ ,  $\sigma_{width}$  is the width of the primary spectrum in terms of range, and  $\beta = 0.0012 \text{ mm}^{-1}$  is a constant determined by Bortfeld. The first term in (5) accounts for the approximately linear reduction in fluence of primary protons as a function of depth, which is a result of primary protons being lost due to inelastic reactions with the target. Whilst the width of the primary beam does depend on depth in the target, it is sufficient to approximate it as a constant [5].

The probability of a secondary being produced at an angle  $\zeta$  to the beam axis is  $P(\zeta)$ . The probability of producing a secondary with range  $r = |\vec{x} - \vec{z}| + \tilde{r}$  is  $D(r)$ . The two quantities are not necessarily independent of one another.

Since we have azimuthal symmetry, we consider the fluence through a thin ring of width  $d\lambda$  and radius  $\lambda$ . The elemental area is  $2\pi\lambda d\lambda$ . The fluence of secondary protons from  $\vec{z}$  through this ring is therefore

$$\frac{2\pi\lambda d\lambda \cos(\zeta)}{|\vec{x} - \vec{z}|^2} = \frac{2\pi\lambda x_z d\lambda}{((x_z - z)^2 + \lambda^2)^{3/2}}, \quad (6)$$

where  $x_z$  is the  $z$  component of  $\vec{x}$ .  $\phi_{\tilde{r}}(\lambda, x_z)$  may therefore be expressed as

$$\phi_{\tilde{r}}(\lambda, x_z) = \int_0^{R_0} dz \frac{2\pi\lambda x_z d\lambda}{((x_z - z)^2 + \lambda^2)^{3/2}} \int d\rho' \sigma(\rho') \phi_p(\rho', z) D(r) P(\zeta). \quad (7)$$

To proceed, the forms of  $\sigma(\rho)$ ,  $D(r)$ , and  $P(\zeta)$  must be determined.

We now consider an elastic reaction in the centre of mass frame between a stationary proton and a proton from the beam of primaries, as illustrated in Figure 2. The total kinetic energy in the laboratory frame is equal to the kinetic energy of the primary proton,  $\mathcal{E}$ . In the centre of mass frame, the kinetic energy is divided equally between the protons after the collision. The kinetic energy of the secondary proton,  $E$ , in the laboratory frame can be related to the total energy in the centre of mass frame via the scattering angle [10]:

$$E = \mathcal{E} \sin^2 \psi = \mathcal{E} \cos^2 \zeta. \quad (8)$$

The Bortfeld relationship may be used to express (8) in terms of the range rather than energy:

$$r = \rho \cos^{2p} \zeta. \quad (9)$$

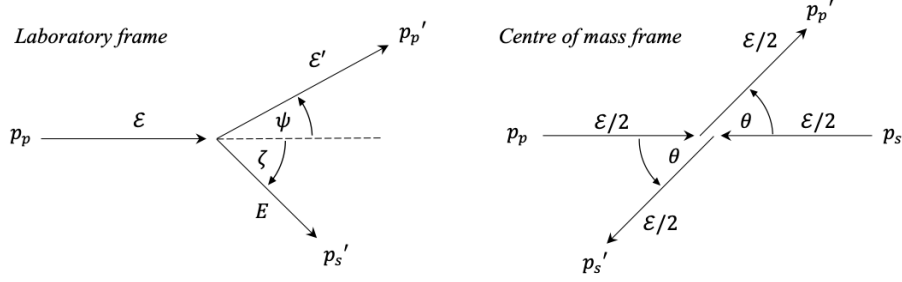


Figure 2: Illustration of the elastic scattering of two protons. The unprimed and primed quantities represent those before and after the collision, respectively, whilst the  $p_p$  and  $p_s$  label the primary and secondary protons with their associated kinetic energies  $\mathcal{E}$  and  $E$ , respectively. Illustration adapted from [10].

To produce a secondary proton with range  $r$  we therefore require a primary proton with range

$$\rho = r \cos^{-2p} \zeta. \quad (10)$$

Since there is a unique relationship between range and the angle of the secondary, (7) can be written

$$\phi_{\bar{r}}(\lambda, x_z) = \int_0^{R_0} dz \frac{2\pi\lambda x_z d\lambda}{((x_z - z)^2 + \lambda^2)^{3/2}} \int d\rho' \sigma(\rho') \phi_p(\rho', z) \delta(\rho' - \rho) P(\zeta). \quad (11)$$

Applying the property of the delta function that  $\int f(x')\delta(x' - x)dx' = f(x)$ ,

$$\phi_{\bar{r}}(\lambda, x_z) = \int_0^{R_0} dz \frac{2\pi\lambda x_z d\lambda}{((x_z - z)^2 + \lambda^2)^{3/2}} \sigma(\rho) \phi_p(\rho, z) P(\zeta). \quad (12)$$

### 3 Monte Carlo simulation

#### 3.1 GEANT4 Overview

GEANT4 version 10.06.02 is a C++ toolkit for the simulation of the passage of particles through matter. A brief overview of the general particle tracking algorithm is given below.

Particles are instantaneously generated at the source and propagate through the medium in a series of steps, whose lengths are distributed exponentially according to the mean free path of the particle, losing energy with each step. At the end of a step, some physics process may happen, such as elastic or inelastic reactions, decays, bremsstrahlung and other processes. The cross sections and reaction products are parameterised by a variety of models defined by the physics list chosen by the user. A physics process may produce secondary particles that

are simulated in a similar manner to the primary particle. Each particle is tracked down until it has zero energy, where it is killed.

The user may design how the particles are created, the simulation geometry, how particles are detected, and how various quantities such as energy deposited are scored and processed.

### 3.2 Simulation Details

The `QGSP_BIC` physics list was chosen, which uses the binary cascade [11] to model low energy hadronic interactions, such as elastic interactions between protons. This is the recommended physics list for medical applications [12]. The only change to the physics list was to reduce the electron production threshold cut from 1 mm to 0.1 mm, as recommended in the authors' previous works [8]. The threshold cut is the minimum range that secondary electrons must be created with in order to be tracked by the simulation. If an electron is created with range below the threshold, its kinetic energy is deposited locally instead.

Two simulation geometries were used: one for measuring the LET of the secondary protons in water for the purpose of comparing the model with data, and one for measuring the angular distribution of the secondary protons so that the quantities  $P(\zeta)$  and  $\sigma(\rho)$  could be determined. The two geometries are shown in Figure 3.

In Figure 3 a), protons travel in the  $+z$  direction (left to right) in a water phantom with dimensions  $50 \times 50 \times 170$  mm. LET is measured using method 3 described in Granville and Sawakuchi [13]. The fluence of secondary protons passing through planes spanning the  $x - y$  dimension spaced 1 mm apart is recorded as a function of the residual range, so that LET may be calculated as a function of depth using (3). Water is used as a proxy for human biological tissue.

In Figure 3 b), protons are generated inside a small sphere of water. They then propagate through a low density nitrogen gas ( $0.005 \text{ g mol}^{-1}$ ). The gas is low density enough that the protons do not interact with it or lose energy as they travel through it. They then reach the curved detector which spans  $[-\pi/2, \pi/2]$  in the  $\theta$  direction. Here the positions of the secondary protons are recorded and the angle between the beam axis and the proton is calculated. If the radius of the sphere is significantly smaller than the inner radius of the detector, the sphere approximates a point and the angular distribution of secondary protons is found. The sphere must also be small such that secondary protons produced at large angles (which have low range) can escape the sphere. To this end, the sphere had a radius of 0.5 mm, and the inner radius of the detector was 20 mm.

In both cases the primary beam had no spatial or energetic width.

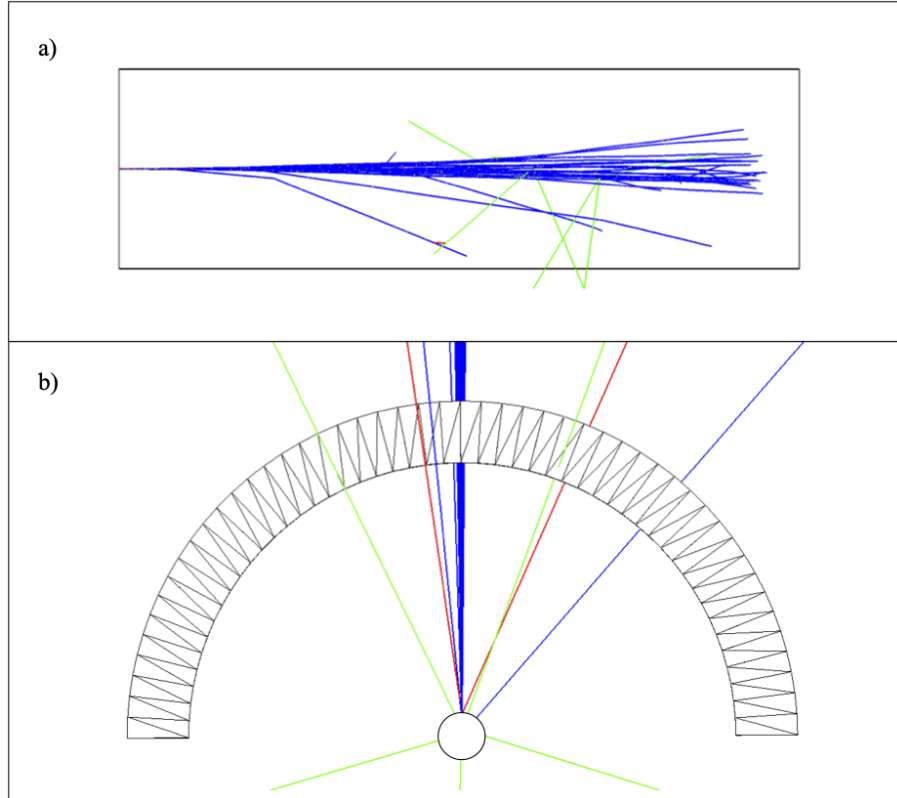


Figure 3: a) Screenshot from GEANT4 interactive mode showing the simulation geometry for measuring LET. b) Simulation geometry for measuring the angular distribution of secondary protons. Note that the sphere has been made larger here for clarity.

Blue, red, and green line segments represent the trajectories of protons (both primary and secondary), electrons, and gammas, respectively.



## 4 Results

### 4.1 Verifying the range-angle relationship

In order to verify (9), the range  $r$  of secondary protons produced in elastic collisions between a water phantom and a 100 MeV beam of primary protons was plotted against the scattering angle  $\zeta$ .

Figure 4 demonstrates that the majority of secondary protons adhere to (9); however, there exist some protons with small  $\zeta$  that do not have the predicted range. This is likely due to some protons making multiple interactions within the spherical phantom, whilst (9) only describes single interactions.

### 4.2 Obtaining $P(\zeta)$ and $\sigma(\rho)$

To obtain  $P(\zeta)$ , a histogram of the number of secondary protons created at an angle  $\zeta$  to the beam axis for a given primary proton energy was created. This was done at three primary proton energies: 150, 100, and 50 MeV. Figure 5 illustrates this. Note that the lower energy curves are cut off at larger angles. This is due to the fact that the secondary protons produced at large angles have very low range, and so they cannot escape the spherical phantom. Moreover, since the sphere is not in fact a point, and so interactions may not all take place at the same location, the cutoff is not sharp, and instead there is a smooth attenuation of secondary protons reaching the detector. This also explains why there appears to be a discrepancy in the height of the curves, since they are normalised by area. However, since the proton spectrum appears in the top and bottom of (3), a constant scaling factor is irrelevant, assuming the same distribution for  $P(\zeta)$  is used for all energies. The Python method `scipy.interpolate.interp1d` [14] with cubic interpolation was used on the 100 MeV data to obtain a function that could be inserted into (3).

To obtain  $\sigma(\rho)$ , a similar experiment to that for  $P(\zeta)$  was carried out, but instead the number of secondary protons reaching the detector as a function of primary proton energy was measured, and then transformed into a function of  $\rho$ . This is proportional to the cross section for elastic reactions, and as before we are not interested in the absolute value of the cross section, only how it varies with energy. This is shown in Figure 6. The cross section depends strongly on energy and is larger for low energies.

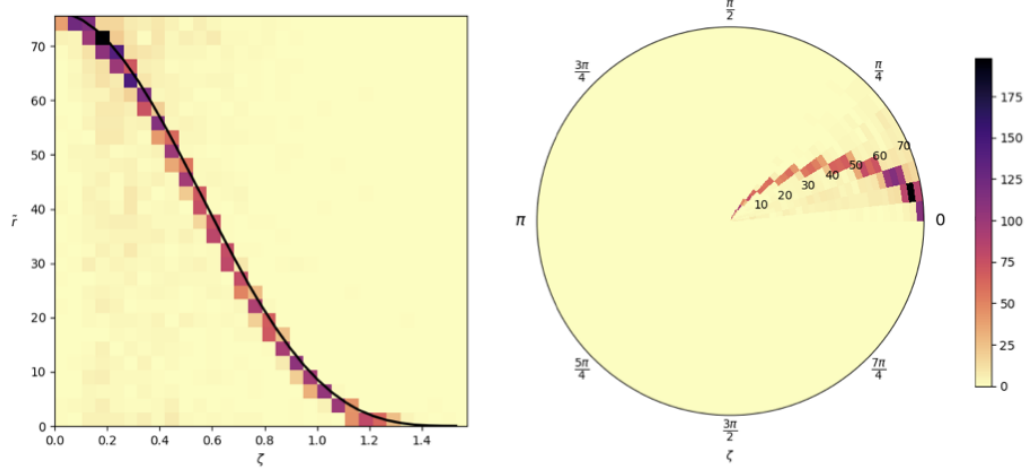


Figure 4: *Left*: Rectilinear 2D histogram of  $r$  against  $\zeta$  for a 100 MeV beam of protons. The black line is the equation  $r = \rho \cos^{2p}\zeta$ . *Right*: The same histogram in polar coordinates. The colourbar gives the frequency of scattering events in a given bin.

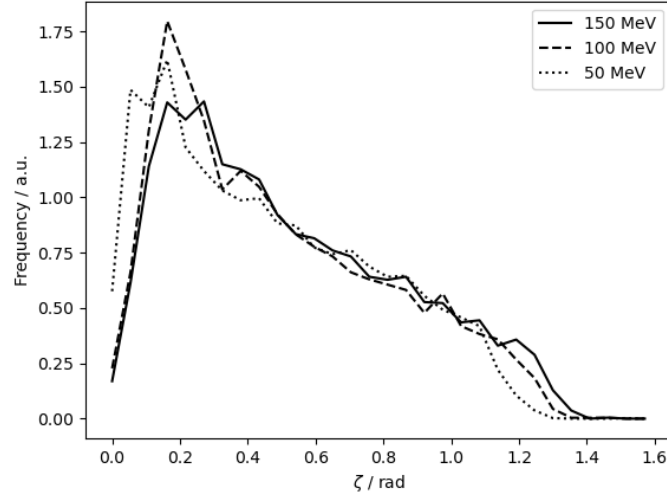


Figure 5: Histogram of angle  $\zeta$ . The curves have been normalised such that the area under each is unity.

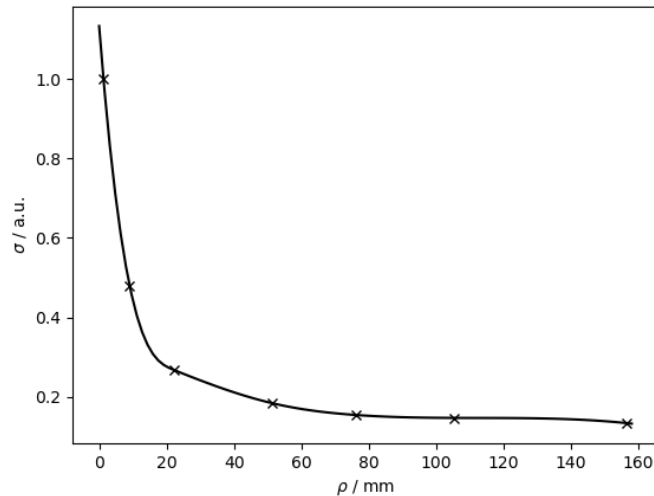


Figure 6:  $\sigma$  as a function of  $\rho$ . The curve is the result of the cubic interpolation.

### 4.3 Beam divergence and multiple Coulomb scattering

In section 2 we assumed that all elastic reaction occurred along the beam axis. To test the validity of this assumption, the total fluence  $\Phi$  through a ring is plotted as a function of the radius of the ring at depths of 80 mm and 150 mm, with the physics process `msc` (corresponding to multiple Coulomb scattering) activated and deactivated in GEANT. This is shown in Figure 7. Note that at 80 mm,  $\Phi$  is similar with and without multiple Coulomb scattering; however, at the end of the beams range, there is a significant difference between the two curves. Multiple Coulomb scattering causes the beam to diverge and so the elastic reactions happen off-axis, and so the secondary protons are further off-axis too. Results obtained by Resch *et al.* by fitting a Gaussian to the central part of the lateral beam profile showed that a 150 MeV beam of protons at the end of its range had a width of 4 mm [15], which is of the same order of magnitude as the difference in  $\lambda$  between the peaks of the two curves corresponding to a measurement depth of 150 mm in Figure 7.

It is therefore clear that at the end of the beam's range, where the LET contribution of secondary protons is most significant, the assumption that beam divergence plays a negligible role is invalid. The beam used in the simulation was perfectly collimated, whilst realistic beams may have an angular divergence of a few milliradians and a spatial width of a few millimetres [16]. Therefore in a simulation with a more realistic beam, divergence would be even more pronounced.

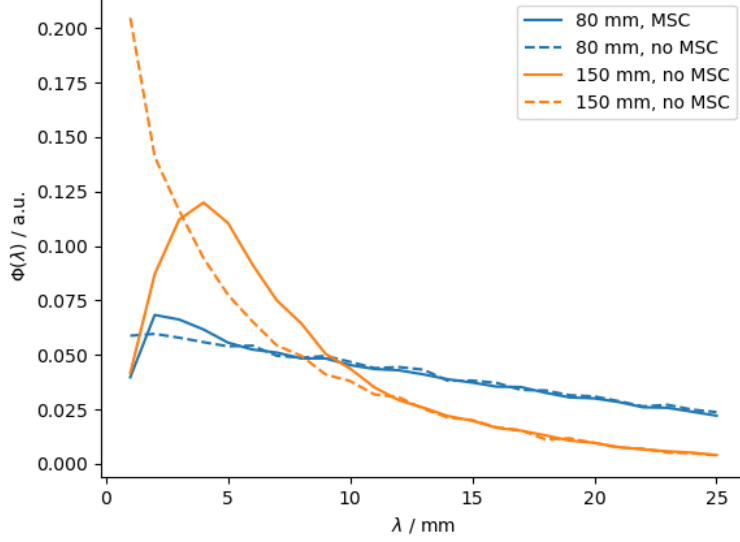


Figure 7:  $\Phi$  as a function of  $\lambda$  at two depths in the water phantom. The curves are normalised to have area unity.

#### 4.4 Secondary proton spectra and LET

A comparison between secondary proton spectra at three depths in the phantom predicted by the model and those from the simulation is shown in Figure 8. In the entrance region and the plateau region (30 mm and 80 mm into the phantom), the model overestimates the number of secondary protons with a high residual range, and significantly underestimates the number with a low residual range. The behaviour of the model at very low residual ranges also does not fit the data well. The data appears to diverge as the residual range goes to zero, whilst the model predicts that the fluence of low range secondary protons decreases with residual range. In the Bragg peak region (150 mm), the model also does not capture the shape of the spectrum well, underestimating the number of low range secondary protons. The maximum range is well predicted by the model, however, showing at worst a discrepancy of 3 mm.

Using (2), LET distributions as a function of depth and  $\lambda$  were calculated. These are shown in Figure 9 and Figure 10, respectively. As a function of depth, the model peaks 2 mm before the Monte Carlo data, and underestimates the LET in the plateau region by a factor of 2. This is even more pronounced in the entrance region, where the Monte Carlo data shows a sharp increase to  $4.3 \text{ keV } \mu\text{m}^{-1}$  whilst the model fails to capture this. The maximum LET is similar in the Bragg peak region, differing by a factor of 5 %.

As a function of  $\lambda$ , the Monte Carlo data shows increasing LET with  $\lambda$ ,

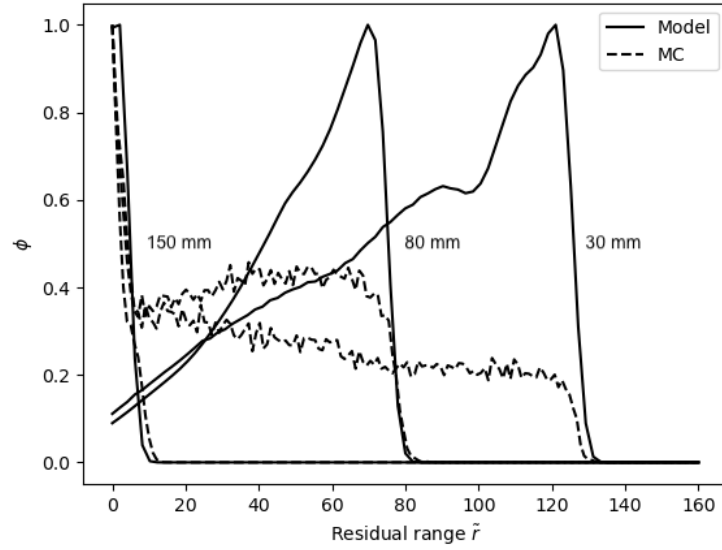


Figure 8: Secondary proton spectra through a plane spanning the  $x-y$  direction at three depths in the water phantom. The model is shown with the continuous line, whilst the broken line shows the data acquired from the Monte Carlo simulation. All curves have been normalised by scaling according to their maximum value.

particularly at a depth of 150 mm into the phantom. The model also shows this trend, however at 80 mm the LET is significantly underestimated, whilst at 150 mm, the increase in LET with  $\lambda$  is too steep.

## 5 Discussion

The model clearly does not describe well the secondary proton spectra, and therefore the LET distributions are also poorly modelled. The explanation for why is either that the mathematical formulation is incorrect, or the model does not include some physical phenomenon that has a significant impact on the proton spectra. We consider some of these reasons below.

The model only accounts for secondary protons produced by primary protons, but not tertiary protons (i.e. protons produced in elastic reactions between secondary protons and the water phantom). These are included in the Monte Carlo simulation, however. This could explain why the model underestimates the number of low range protons, since tertiary protons will have less energy than the secondary protons that created them. This argument becomes more compelling considering that the cross section for elastic reactions increases with decreasing proton energy, suggesting that secondary protons are more likely to produce tertiary protons, which are then likely to produce quaternary protons etc. However, low range protons do not travel far in the phantom, and so the probability of a collision is small. This effect can be seen by running the Monte Carlo simulation again but excluding protons that were not created by an elastic reaction with a primary proton. The difference in the total number of protons recorded is less than 1%. It is therefore unlikely that this is the main cause of the large discrepancy between the model and the Monte Carlo data.

The model does not account for range straggling. It assumes that every proton produced at an angle  $\zeta$  will travel a distance  $r = \rho \cos^{2p}\zeta$ . In reality, the distance travelled will be distributed about  $r$ . This is due to the fact that each proton will take a slightly different path due to the statistical nature of the transport process. A consideration of range straggling is seen in Bortfeld [4] Appendix A, by convolving the range term with a Gaussian distribution. A similar treatment could be applied to our model. It is unlikely to significantly increase the number of low range secondary protons, however. By introducing range straggling, one expects the proton spectra to be “smeared”. We require some mechanism to increase the number of low range protons, but the symmetry of the Gaussian distribution implies that there will be an equivalent number of secondary protons with range greater than  $r$  as less than  $r$ .

The integration must be carried out numerically, since  $P(\zeta)$  and  $\sigma(\rho)$  are calculated using lookup tables. In order to calculate a full spectrum in two dimensions (depth and  $\lambda$ ), many such integrals must be calculated. In the water phantom, the local secondary proton spectrum was calculated at 1 mm intervals between 0 and 160 mm in the  $z$  direction, and between 0 and 25 mm in the  $\lambda$  direction, spaced 1 mm apart, resulting in 4000 integrals to be calculated. This is a time consuming process: using a 2.7 GHz Dual-Core Intel Core i5 processor,

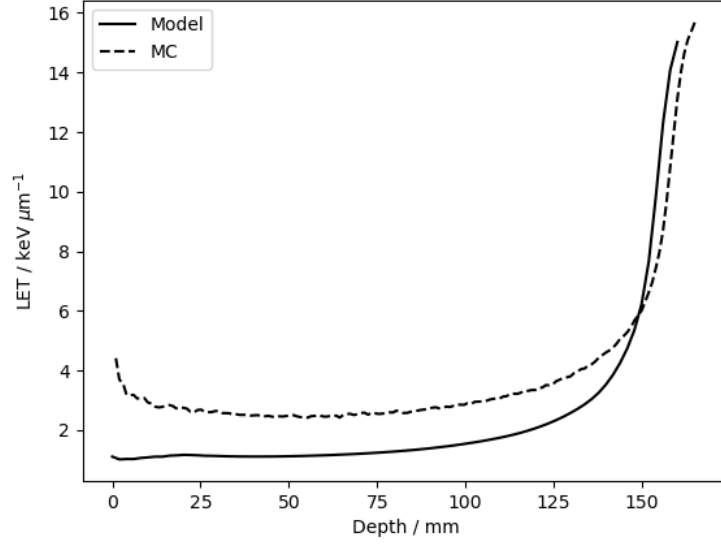


Figure 9: Secondary proton spectra LET as a function of depth in the water phantom, using the model and the Monte Carlo simulation data.

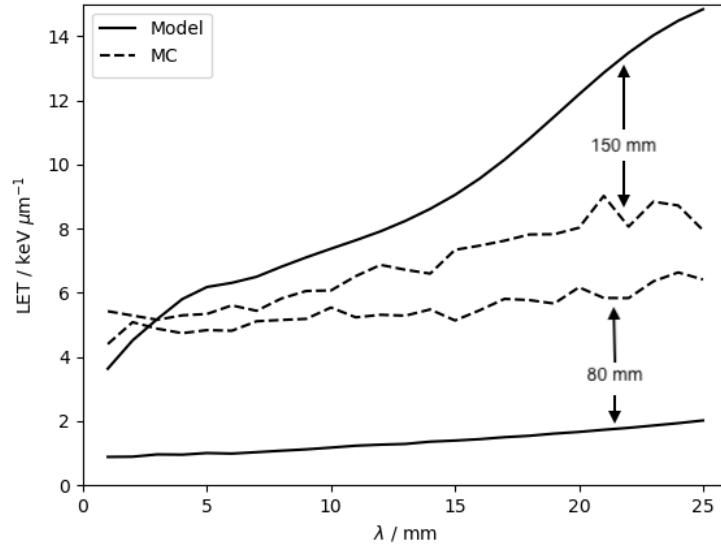


Figure 10: Secondary proton spectra LET as a function of  $\lambda$  in the water phantom, calculated at two depths (80 and 150 mm), using the model and the Monte Carlo simulation data.

a full calculation takes nearly 20 minutes. Whilst this is an improvement over performing a Monte Carlo simulation which can take over an hour, optimising a treatment plan using the model would still take a potentially prohibitive amount of time. However, in a clinical setting, the entire geometry may not be of interest, since biological effect is generally small where there is little dose deposited. Therefore the model can be used in a small area without having to calculate the integral for the entire geometry. This is a significant decrease in computation time, and a clear advantage over the Monte Carlo simulation. Moreover, if an analytical model for  $P(\zeta)$  and  $\sigma(\rho)$  could be found, or at least a suitable approximation, the integral may have a closed form solution. This would result in the most drastic decrease in computation time.

It was shown that beam divergence cannot be ignored, especially towards the end of the beam's range. Beam divergence could be incorporated into the model by finding an analytical representation for the beam width as a function of depth, and then integrating over the width of the beam. By permitting the primary beam to diverge, the model could also accommodate more realistic beam geometries. However, adding another integral into the model would slow it down further.

The model only includes secondary protons produced in elastic reactions. In order to extend the model to include those produced in inelastic reactions, a parameterization for the angular and energy distributions must be found. Inelastic reactions are generally isotropic in the centre of mass frame [17], and then this could be transformed into the laboratory frame to obtain an angular distribution. Along with an expression for the energy distribution, (7) could be extended to include inelastic secondary protons. Since there does not exist a unique relationship between energy and scattering angle, it would not be possible to collapse the integral as in (12).

## 6 Conclusions

We devised a novel model for the local secondary proton spectrum from protons produced in elastic reactions that could then be converted into an LET distribution. The model agreed poorly with the data, and consequently the LET distributions were also poorly described. Potential reasons for the significant discrepancy between data collected from Monte Carlo simulations and the model were discussed, as well as ways to extend the model to include secondary protons from inelastic reactions.

Despite the shortcomings of the model, its advantage in terms of speed was significant compared to a full Monte Carlo simulation. In addition, since the spectrum in a small region of interest can be calculated independently of the rest of the geometry, a treatment plan could be optimised quickly in order to avoid excessive biological damage in sensitive areas. For example, when treating breast cancer, damage to the lungs needs to be minimized. It is therefore imperative that the LET at the end of the beam's range can quickly and accurately be modelled.



## References

- [1] H. Paganetti, A. Niemierko, M. Ancukiewicz, L. E. Gerweck, M. Goitein, J. S. Loeffler, and H. D. Suit, “Relative biological effectiveness (RBE) values for proton beam therapy,” *Int J Radiat Oncol Biol Phys*, vol. 53, no. 2, pp. 407–21, 2002.
- [2] T. Friedrich, U. Scholz, T. Elsässer, M. Durante, and M. Scholz, “Systematic analysis of rbe and related quantities using a database of cell survival experiments with ion beam irradiation,” *Journal of Radiation Research*, vol. 54, pp. 494–514, 2013.
- [3] E. Rørvik, L. F. Fjæra, T. J. Dahle, J. Dale, G. M. Engeseth, C. H. Stokkevang, S. Thörnqvist, and K. S. Ytre-Hauge, “Exploration and application of phenomenological rbe models for proton therapy,” *Physics in Medicine and Biology*, vol. 63, 2018.
- [4] T. Bortfeld, “An analytical approximation of the bragg curve for therapeutic proton beams,” *Medical Physics*, vol. 24, no. 12, pp. 2024–2033, 1997.
- [5] J. J. Wilkens and U. Oelfke, “Analytical linear energy transfer calculations for proton therapy,” *Medical Physics*, vol. 30, no. 5, pp. 806–815, 2003.
- [6] C. Grassberger and H. Paganetti, “Elevated LET components in clinical proton beams,” *Phys. Med. Biol.*, vol. 56, no. 20, p. 6677, 2011.
- [7] D. Sanchez-Parcerisa, M. A. Cortés-Giraldo, D. Dolney, M. Kondrila, M. Fager, and A. Carabe, “Analytical calculation of proton linear energy transfer in voxelized geometries including secondary protons,” *Phys. Med. Biol.*, vol. 61, no. 4, p. 1705, 2016.
- [8] B. White and Project Partner, “Analytical model for the linear energy transfer of secondary protons in proton beam therapy,” 2021.
- [9] *Fundamental quantities and units for ionizing radiation*, vol. 11 of *ICRU Report 85*. Bethesda, MD: ICRU, 2011.
- [10] R. Fitzpatrick, “Scattering in the laboratory frame,” 2011. <http://farside.ph.utexas.edu/teaching/336k/Newtonhtml/node52.html>.
- [11] G. Folger, V. N. Ivanchenko, and J. P. Wellisch, “The binary cascade,” *European Physical Journal A - Hadrons and Nuclei*, vol. 21, pp. 407–417, 2004.
- [12] D. Wright and S. Incerti, “A short guide to choosing a physics list,” *Geant4 Tutorial at Jefferson Lab, SLAC*, 2012.
- [13] D. A. Granville and G. O. Sawakuchi, “Comparison of linear energy transfer scoring techniques in monte carlo simulations of proton beams,” *Phys. Med. Biol.*, vol. 60, p. 283, 2015.

- [14] The SciPy Community, “scipy.interpolate.interp1d,” 2021. <https://docs.scipy.org/doc/scipy/reference/generated/scipy.interpolate.interp1d.html>.
- [15] A. F. Resch, A. Elia, H. Fuchs, A. Carlino, H. Palmans, H. Stock, D. Georg, and L. Grevillot, “Evaluation of electromagnetic and nuclear scattering models in gate/geant4 for proton therapy,” *Medical Physics*, vol. 46, 2019.
- [16] H. Paganetti, “Proton beam therapy,” 2399-2891, p. 6, IOP Publishing, 2017.
- [17] K. S. Krane, *Introductory Nuclear Physics*. Oregon State University: John Wiley & Sons, 1987.